3. Models and Procedures

3.1 Introduction

An analytical model was developed to study linear and nonlinear viscous fluid dampers in structures subjected to earthquake ground motions. The model used includes a 2-D frame with inelastic deformations concentrated at specific points. The model parameters were selected to provide the most accurate representation of a structure's behavior within a reasonable amount of computational time. Using this model in conjunction with a new analysis method called Incremental Dynamic Analysis, this study has accomplished the objectives presented in Chapter 1.

3.2 Description of Model

This study requires the use of nonlinear dynamic time history analysis in order to observe the effects of linear and nonlinear dampers on structural response to earthquake ground motions. A new structural analysis program called *RAM Perform 2D* (Powell, 2000) was selected to run the analysis because, at the start of the study, it was the only commercial program that had the combined capabilities of nonlinear inelastic time history analysis and use of nonlinear viscous damper elements. According to the *Perform* users guide, the nonlinear time history analysis is executed using a step-by-step integration through time, using the constant average acceleration method (also known as the Newmark β method with $\beta=1/4$). The following sections describe the model that was used in this study and explain how the inelastic response is modeled for each element.

3.2.1 Introduction to LA 9-Story Building

The model that was used in this study is a model of the LA 9-story building designed for the SAC building project (Gupta and Krawinkler, 1999). Instead of designing a new building, the moment-resisting frame of this building was selected for various reasons. One reason is that this building was designed so that it will perform inelastically when it is subjected to seismic loads that range from moderate to severe. This is essential for the

analysis because the role of the dampers is to reduce the amount of hysteretic energy dissipated by structural elements, and hysteretic energy is caused by repeated inelastic deformations. Another reason is that this building has been studied extensively over the last few years through the SAC steel project; therefore there are a number of models available for making comparisons to check the validity of the model used in this study. A final reason the design was used is that it is known that this building will behave undesirably during earthquakes and the results of the analysis will determine if viscous dampers are able to reduce the undesirable behavior.

The building design used for the model is nine stories with one sublevel and five bays in each direction. A plan view of the building can be seen in Figure 3.1. From the plan view the moment-resisting frames, which are the lateral force resisting system, are the exterior frames of the building, while the gravity frames are located in the interior. This building has 4 moment-resisting frames, 2 in each direction. The model in this study will consist of just one of these moment-resisting frames.

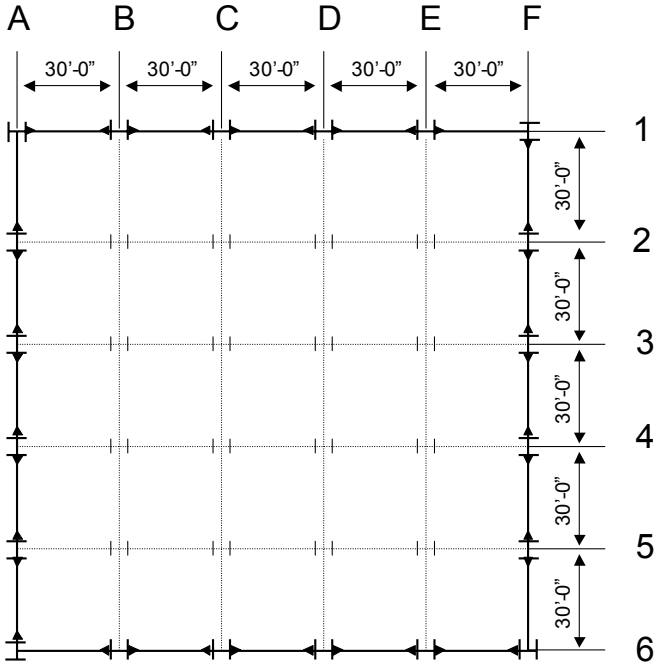

Figure 3.1: Plan View of LA 9-Story Building

Figure 3.2 illustrates the elevation of the frame on Column Line 1 including member sizes for each beam and column. It is important to note that the columns at Line F will bend about their weak axis when subjected to in-plane forces. Furthermore, the connection of the rightmost girder to the column is not a moment connection, but instead just a pin connection. The rest of the connections are moment connections, and the beam-to-column joints have been modeled using the Krawinkler model (Gupta and Krawinkler, 1999).

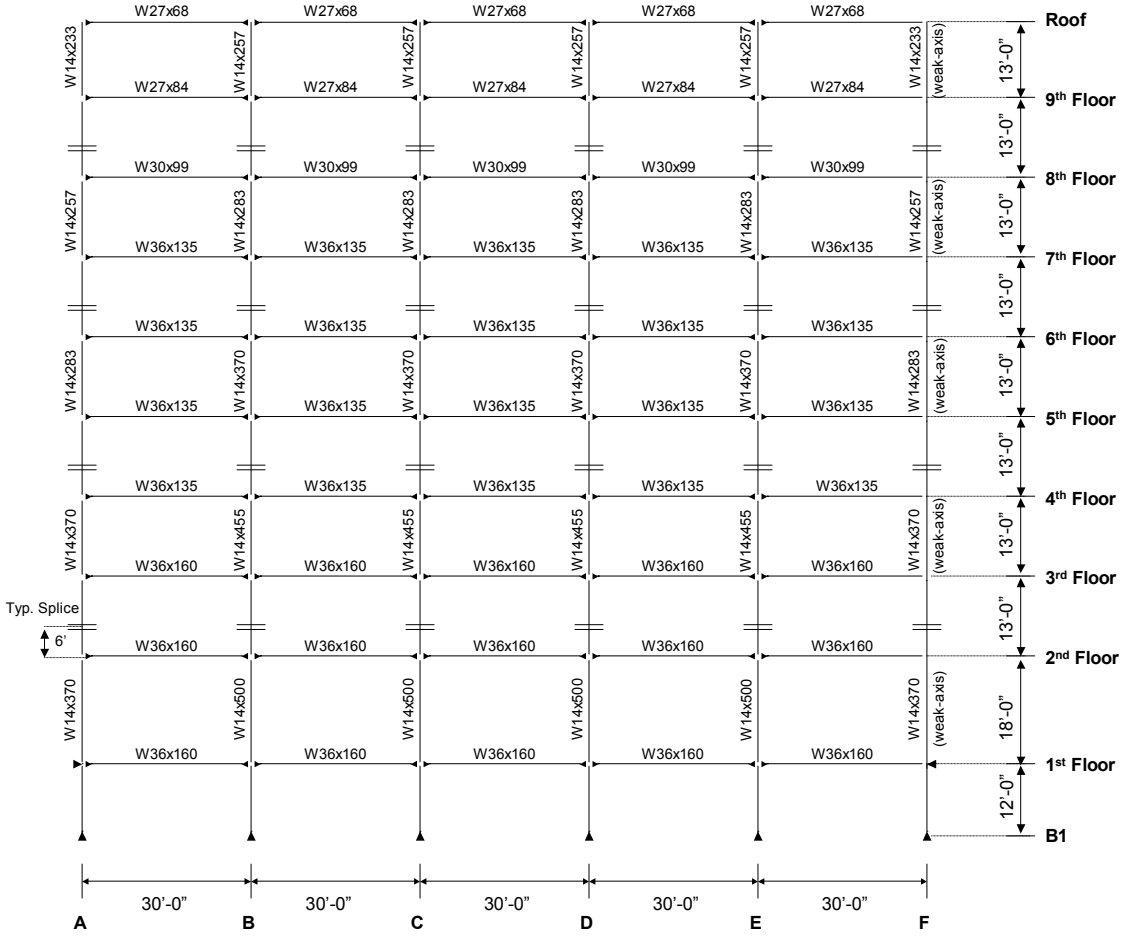

Figure 3.2: LA 9-Story MRF (N-S Elevation)

The design for the 9-story building was completed using the specification in use prior to the Northridge earthquake; therefore none of the panel zones were designed with doubler plates. This was done intentionally because it ensures that the structure undergoes sufficient yielding and it provided undesirable behavior that the damping systems could correct.

The cross-sectional properties of each beam and column are listed in Table 3.1. The yield strengths for the beams and columns are the expected strengths when the nominal strengths are 36 ksi and 50 ksi, respectively. The expected strengths were used because a model developed for previous research by Gupta and Krawinkler (1999) used the expected strengths and their model was used as a check. It is also important to note that shear deformations were included in this model. Shear deformations may be ignored when they are small relative to flexural deformations. However, for a 9-story building, including shear deformations can significantly affect the overall stiffness and period of the building. In Table 3.1, A' is the shear area of the beams and columns and ν is Poisson's ratio.

Table 3.1: Section Properties

Beams	F_y (ksi)	E (ksi)	I (in^4)	A (in^2)	A' (in^2)	ν
W36x160	49.2	29000	9750	47	23.406	0.3
W36x135	49.2	29000	7800	39.7	21.33	0.3
W30x99	49.2	29000	3990	29.1	15.418	0.3
W27x84	49.2	29000	2850	24.8	12.287	0.3
W24x68	49.2	29000	1830	20.1	9.848	0.3
Columns	F_y (ksi)	E (ksi)	I (in^4)	A (in^2)	A' (in^2)	ν
W14x500	57.6	29000	8210	147	42.924	0.3
W14x455	57.6	29000	7190	134	38.325	0.3
W14x370	57.6	29000	5440	109	29.658	0.3
W14x370 (weak)	57.6	29000	1990	109	73.054	0.3
W14x283	57.6	29000	3840	83.3	21.595	0.3
W14x283 (weak)	57.6	29000	1440	83.3	55.591	0.3
W14x257	57.6	29000	3400	75.6	19.246	0.3
W14x257 (weak)	57.6	29000	1290	75.6	50.394	0.3
W14x233	57.6	29000	3010	68.5	17.163	0.3
W14x233 (weak)	57.6	29000	1150	68.5	45.56	0.3

3.2.2 Beams

The beams of the building were modeled using three components: linear elastic beam segments, inelastic point hinges, and rigid end zones as shown in Figure 3.3. In the analysis, it was expected that any inelastic response in the beams would be due to lateral loads instead of gravity loads. This would result in inelastic deformations located in a region near the face of the column rather than the mid-span. When subjected to seismic loading this plastic region may grow and shift closer or further from the column face. In *Perform,* the plastic region is simplified as a point at a fixed distance from the column face in the form of inelastic hinges. The hinge location is approximate, but according to Gupta and Krawinkler (1999), it is valid because the behavior of the building is relatively insensitive to hinge location. In this study, the hinges were be placed 6 in. from the column face. The rigid end zones were included in the beam model because *Perform* requires them for beams and columns when panel zone deformations are considered in the model. The rigid end zones are not be part of the beam, but instead part of the beam-to-column connection.

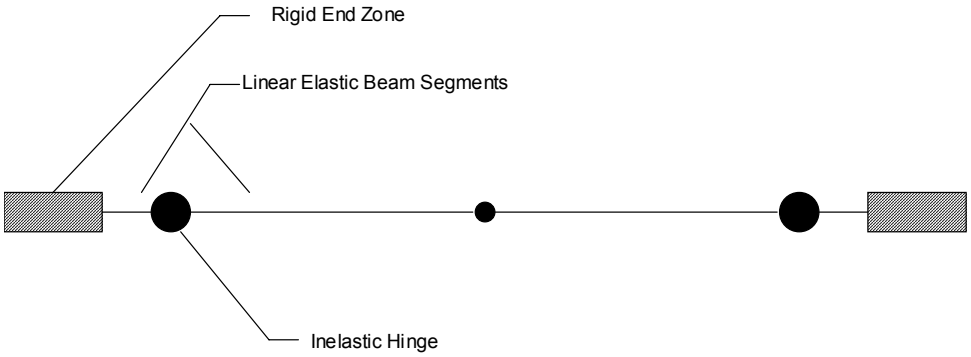

Figure 3.3: Typical Beam Element

Figure 3.3 displays three nodes for each beam element; two of these nodes are compound nodes near the face of the column and the other is a simple node at the mid-span. The

purpose of the mid-span node is to enhance the deflected shape of the structure. The purpose of the compound nodes is to model the inelastic hinges. In *Perform* the inelastic hinges have a moment-rotation relationship shown in Figure 3.4.

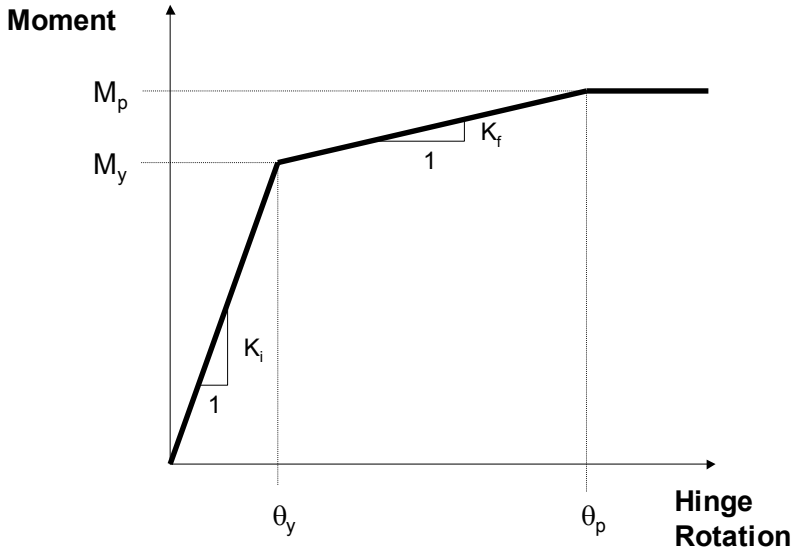

Figure 3.4: Moment-Rotation Relationship for an Inelastic Hinge

This moment-rotation relationship is trilinear and the hinge is perfectly plastic for the last portion of the curve. However, the values for M_p and θ_p are set to large values so that the moment-rotation relationship for the hinge is simplified as a bilinear curve. The initial stiffness of the hinge is large until the hinge yields and then the stiffness decreases significantly. Therefore, the beam will behave as a linear elastic beam with certain cross-sectional properties up until yield, when the beam develops a hinge.

The bilinear moment-rotation relationship for each girder in the model was determined by moment-curvature analysis of the cross-sections, and is a function of the stress-strain relationship of the steel used in the girders. The assumed stress-strain relationship was simplified as a bilinear curve as illustrated in Figure 3.5 a. The first part of the curve is the linear elastic portion and, after the yield strength is reached, strain hardening provides

the additional stiffness. In steel, strain hardening occurs after the material has yielded and passed through a region known as the yield plateau. The hardening is a result of the material's crystalline structure undergoing changes, which results in an increased resistance to further deformation. The stress-strain curve used in the moment-curvature method ignores the yield plateau, which is allowed because it is assumed that the cross-section has yielded in previous cycles. The amount of strain hardening used in this study is 3%.

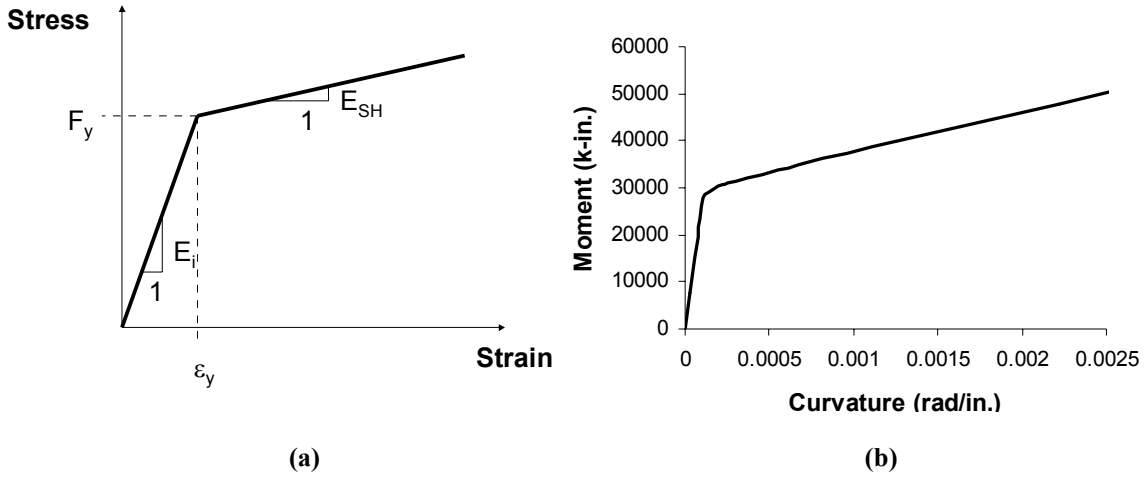

Figure 3.5 (a-b): Stress-Strain and Moment-Curvature Relationships

With the bilinear stress-strain curve, a moment-curvature relationship for each cross-section was then determined using equilibrium and strain compatibility. This is a repetitive process where a value of strain for a fiber can be determined for a given curvature using the strain compatibility assumption that plane sections remains plane. The fiber stress can then be determined using the stress-strain relationship previously defined. Next, the moment for a given curvature is calculated by summing all of the stresses in each fiber multiplied by the area of each fiber multiplied again by the distance of each fiber to the neutral axis. The location of the neutral axis is found using equilibrium. When steel I-shapes are used, as in this study, the neutral axis is located at the axis of symmetry.

The moment-curvature relationship, as shown in Figure 3.5 b, can also be simplified as a bilinear curve. This curve is then used to generate the moment-rotation relationship for each inelastic hinge. This is accomplished through the analysis of a cantilever beam loaded as illustrated in Figure 3.6. The beams in the structure will experience this loading if it is assumed that there are inflection points at mid-span, which is a reasonable assumption if lateral loads dominate the structure. When loaded in this manner, the moment diagram will be similar to that displayed in Figure 3.7.

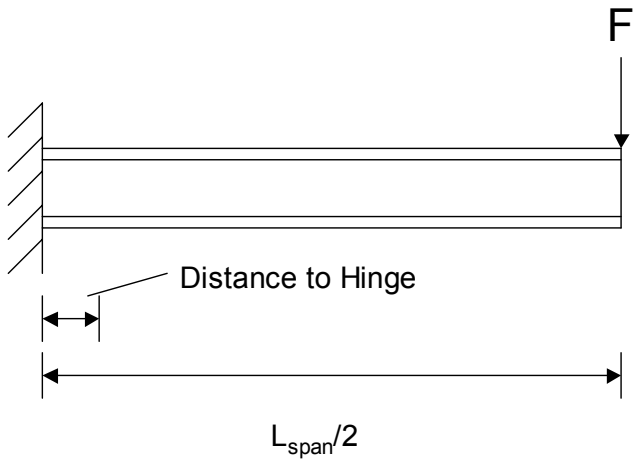

Figure 3.6: Cantilever Beam Analysis

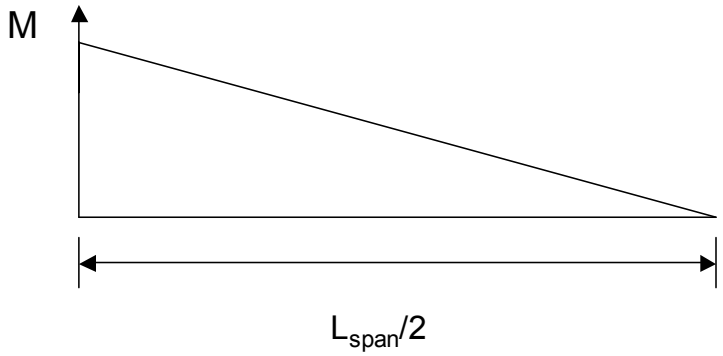

Figure 3.7: Moment Diagram for Cantilever Beam

Once the moment diagram is known, a curvature diagram can be generated using the bilinear moment-curvature relationship previously defined. If the moment along the beam remains in the linear elastic region, then the curvature across the beam will be

distributed similarly to the moment. However, if the moment exceeds the yield moment, then the curvature along the beam will be similar to that shown in Figure 3.8.

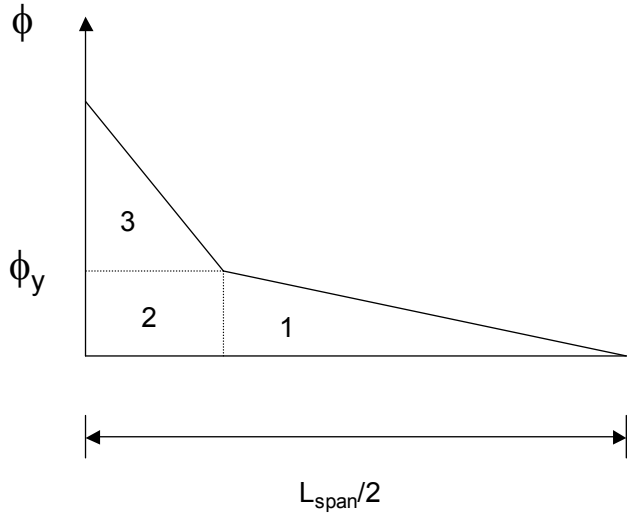

Figure 3.8: Curvature Diagram for Cantilever Beam

The curvature distribution can be used to obtain the deflection at the point of the load with the moment area method. Figure 3.8 shows three different areas. Areas one and two are the elastic portions of the displacement and area three is the inelastic portion. When the load, F, is added, the beam will be linear elastic and deflect according to its cross-sectional properties until the moment at the location of the hinge reaches the yield moment. Once the yield moment is reached, the beam will deform inelastically according to the hinge's moment-rotation relationship. This relationship is obtained by applying load at the end of the beam to create a moment at the hinge. Next, a curvature diagram, as shown in Figure 3.8, is drawn for the beam under the load. Using the moment-curvature diagram, the moment area method can then be used to solve for the inelastic portion of the beam displacement at the end of the beam. This displacement is then divided by the distance from the hinge to the end of the beam in order to get the rotation. This process is repeated until there are enough values of the moment and the rotation to create a curve.

For the model used in this study the moment-rotation relationship was approximated with a bilinear curve as shown earlier in Figure 3.4. Table 3.2 lists the initial stiffness, the yield moment, and the final stiffness for the cross-section of each beam used in this study.

Table 3.2: Moment-Rotation Properties for Inelastic Beam Hinges

Beam	K_i (k-in./rad)	M_y (k-in.)	K_f (k-in./rad)	M_p (k-in.)	θ_p (rad)
W36x160	huge	28408	105347	44210	0.15
W36x135	huge	23134	84640	35830	0.15
W30x99	huge	14425	40847	20552	0.15
W27x84	huge	11336	28400	15596	0.15
W24x68	huge	8278	17453	10896	0.15

3.2.3 Columns

The columns of the structure were modeled similarly to the beams with the following exceptions. The columns are similar to the beams in that they consist of two linear elastic segments with a center node and inelastic hinges near the ends. Furthermore, both elements have rigid end zones, which become part of the inelastic panel zones. The first difference is that the inelastic hinges forms adjacent to the face of the beam-to-column connections. The other difference is that the inelastic hinges incorporate a moment-axial force relationship. Figure 3.9 illustrates the model of the column that is used.

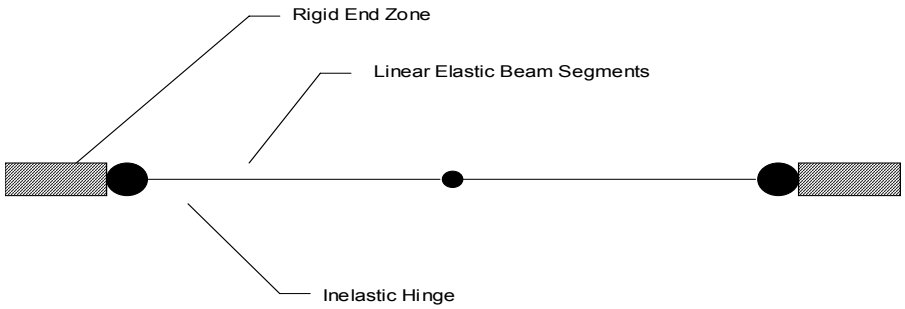

Figure 3.9: Typical Column Element

The columns of the structure are expected to resist significant axial loads, much greater than those experienced in the beams, and because of this, the hinges used will be special P-M hinges, where P stands for axial loads and M stands for moment. As before, these hinges have moment-rotation relationships that were determined using a moment-curvature analysis. Table 3.1 displays the moment-rotation properties for each column. The hinges also include the behavior due to moment-axial load interaction. This causes the hinges to yield under a combined loading of either a moment and a compressive forces or a moment and a tensile force. To account for this, the column hinges were modeled with a P-M interaction similar to that found in Figure 3.10.

Table 3.3: Moment-Rotation Properties for Inelastic Column Hinges

Column	K_i (k-in./rad)	M_y (k-in.)	K_f (k-in./rad)	M_p (k-in.)	θ_p (rad)
W14x500	huge	54386	200900	84521	0.15
W14x455	huge	54015	122720	72423	0.15
W14x370	huge	38585	128787	57903	0.15
W14x370 (weak)	huge	21373	35000	26623	0.15
W14x283	huge	31269	64933	41009	0.15
W14x283 (weak)	huge	15812	23200	19292	0.15
W14x257	huge	28161	56947	36703	0.15
W14x257 (weak)	huge	14195	20780	17312	0.15
W14x233	huge	25200	50413	32762	0.15
W14x233 (weak)	huge	12750	18513	15527	0.15

From Figure 3.10 it can be observed that as the axial load on a column increases, the bending strength decreases or alternately, as the bending moment increases, the axial strength decreases. *Perform* calculates this relationship automatically, and through comparisons with past models of the LA 9-story building (Gupta and Krawinkler, 1999) it was determined that the relationships generated are valid.

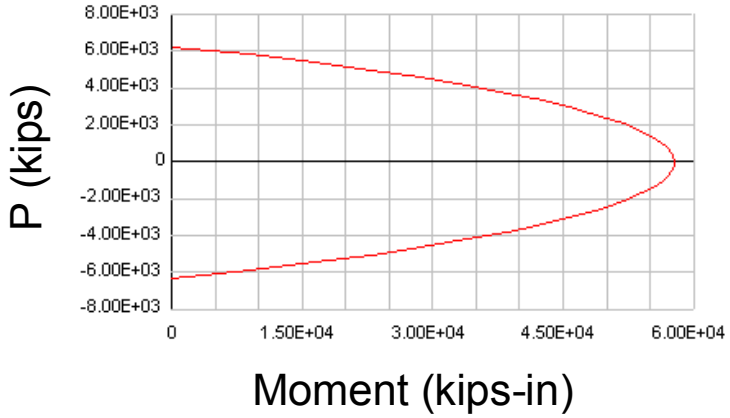

Figure 3.10: P-M Interaction Diagram for Column Hinges

3.2.4 Panel Zones

There are several different methods for modeling the beam-to-column connections. The simplest of these methods is to model the connections as centerline connections. With this model, the beams and columns connect at a point of intersection of the members' centerlines and the panel zones are ignored. While this approach is simple, it may not be conservative. Another simple model similar to the centerline model is the rigid end zone model. This model is similar to the centerline model except that a portion at the end of each beam and column is rigid. This method seems reasonable in that, at the end of the element in the panel zone, the member will have much more flexural stiffness. However, this method is not entirely accurate because the panel zone may still deform in shear.

As moments are transferred between beams and columns large shear stresses are generated in the column portions of the panel zone. These stresses cause the panel zone to deform into a parallelogram shape and the lateral displacements caused by this can be

a significant component to the overall story drift. Therefore, it is important that the panel zones are included in the model of the frame and that they are modeled correctly.

In this study the panel zones were modeled using the Krawinkler model that was first introduced in 1978. The model consists of 12 nodes and as little as four degrees of freedom. An example of this analytical model can be seen in Figure 3.11. As illustrated in the figure, there are four nodes where the beams and columns frame into the panel zone. The panel zone is modeled as four rigid beam segments, which are connected at each of the four corners with two superimposed nodes. These nodes share translation degrees of freedom, but each has its own rotational degree of freedom. At two of the corners, the nodes are connected by rotational springs, which will model the stiffness and strength provided by the panel zone.

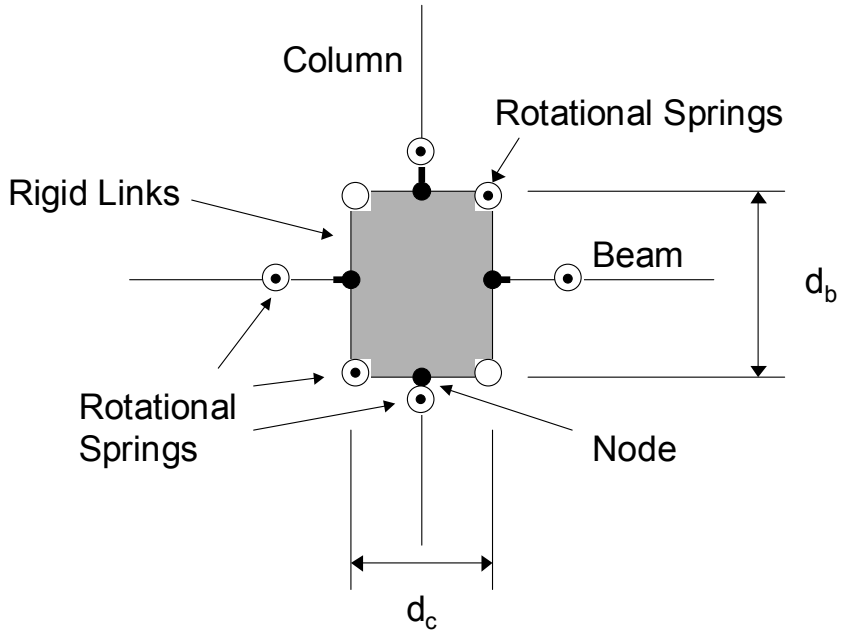

Figure 3.11: Krawinkler Model for the Beam-to-Column Connections

There is a simpler model that could be used, which is called the scissors model. This model is similar to the rigid end zone model except that each element has its own rotational degree of freedom at the node of the connection. With the use of springs to

simulate the rotational stiffness of the panel zone, the beam-to-column connection can be modeled properly. The advantage of this model is that only two nodes are needed and there are only four degrees of freedom, which would decrease the amount of computer processing needed to analysis the structure. However, the current study did not use this model because *Perform* has a built-in Krawinkler panel zone element. Furthermore, while there are superimposed nodes in *Perform's* Krawinkler panel zone element, the restrictions of the program do not allow nodes to be superimposed, which is required to create the scissors model.

The Krawinkler model causes the panel zone to behave according to the shear force-shear strain relationship plotted in Figure 3.12.

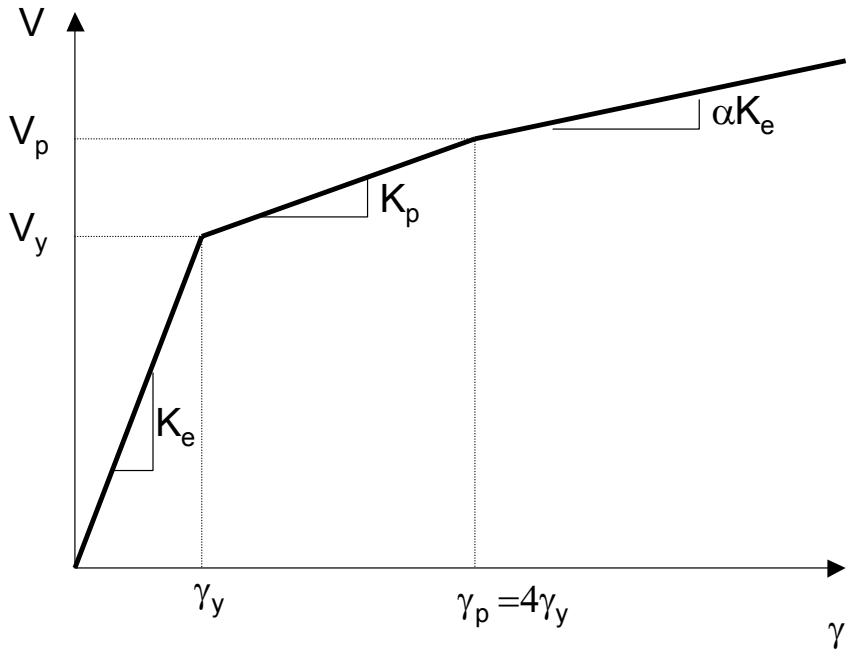

Figure 3.12: Shear Force-Shear Strain Relationship for Panel Zone

To generate the relationship displayed in Figure 3.12 for the panel zone elements used in *Perform,* the following needed to be determined: the initial stiffness of the rotational spring, the yield moment of the rotational spring, the secondary stiffness of the rotational

spring, the moment at the plastic shear strain, and the hardening stiffness due to the column flanges. In this study, these properties were determined using equations derived for a study by Gupta and Krawinkler (1999). These equations were used because these researchers had previously modeled the LA 9-story building and this model was used to check the accuracy of the one used in the current study.

The initial stiffness can be found with the following equation:

$$K_1 = d_b K_e \left(1 - \frac{b_c t_{cf}^2}{d_b d_c t_p} \right) \tag{3.1}$$

where d_b is beam depth, d_c is column depth, t_p is panel zone thickness, b_c is column flange width, t_{cf} is column flange thickness, and K_e can be determined by the following equation:

$$K_e = 0.95 d_c t_p G \tag{3.2}$$

The yield moment is determined from

$$M_1 = K_1 \gamma_{1,y} \tag{3.3}$$

where $\gamma_{1,y}$ is the first yield rotation. This yield rotation can be determined from

$$\gamma_y = \frac{F_y}{\sqrt{3} \times G} \tag{3.4}$$

where F_y is the yield strength and G is the shear modulus of the column material. The secondary stiffness is then found using

$$K_2 = d_d K_e \left(\frac{b_c t_{cf}^2}{d_b d_c t_p} \right) \tag{3.5}$$

By using the secondary stiffness and the second yield rotation, which is equal to 4 times the first yield rotation, the plastic moment can be determined using the following equation:

$$M_2 = M_1 + 3\gamma_{1,y} K_2 \tag{3.6}$$

Finally, the hardening stiffness ratio due to the column flanges is determined as

$$\frac{K_f}{K_1} = \alpha\left(\frac{d_b d_c t_p}{b_c t_{cf}^2}\right)\left(\frac{K_2}{K_1}\right) \qquad 3.7$$

where α=0.3.

These properties will yield moment-rotation relationships similar to that shown in Figure 3.13.

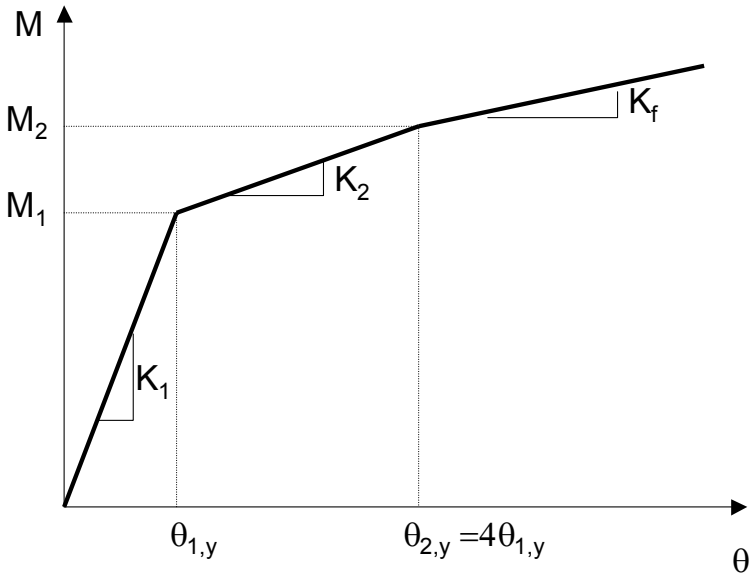

Figure 3.13: Moment-Rotation Relationship for Panel Zone Spring

The panel zone properties for each panel zone used in the structure can be found in Table 3.4. Notice that for each level the properties are not the same for the interior panel zones and the exterior panel zones because the columns framing into the connection are different.

Table 3.4: Panel Zone Hinge Properties

Floor	Location	Beam	Column	K_1 (k-in./rad)	$\gamma_{1,y}$ (rad)	$M_{1,y}$ (k-in.)	K_2 (k-in./rad)	$\gamma_{2,y}$ (rad)	$M_{2,y}$ (k-in.)	α
1st & 2nd	Ext	W36x160	W14x370	10081316	0.00298	30140	1651511	0.0119	44912	0.034
	Int	W36x160	W14x500	14170652	0.00298	42366	2952113	0.0119	68771	0.035
3rd	Ext	W36x160	W14x370	10081316	0.00298	30140	1651511	0.0119	44912	0.034
	Int	W36x160	W14x455	12785756	0.00298	38226	2457627	0.0119	60208	0.034
4th	Ext	W36x135	W14x370	9936756.3	0.00298	29708	1651511	0.0119	44480	0.034
	Int	W36x135	W14x455	12598947	0.00298	37667	2457627	0.0119	59649	0.034
5th & 6th	Ext	W36x135	W14x283	7403192.8	0.00298	22133	977978	0.0119	30881	0.033
	Int	W36x135	W14x370	9936756.3	0.00298	29708	1651511	0.0119	44480	0.034
7th	Ext	W36x135	W14x257	6644699.6	0.00298	19866	809470	0.0119	27106	0.033
	Int	W36x135	W14x283	7403192.8	0.00298	22133	977978	0.0119	30881	0.033
8th	Ext	W30x99	W14x257	5441443.6	0.00298	16268	809470	0.0119	23509	0.033
	Int	W30x99	W14x283	6053138	0.00298	18097	977978	0.0119	26845	0.034
9th	Ext	W27x84	W14x233	4359417.6	0.00298	13033	665999	0.0119	18990	0.033
	Int	W27x84	W14x257	4841855	0.00298	14476	809470	0.0119	21716	0.034
Roof	Ext	W24x68	W14x233	3817468.3	0.00298	11413	665999	0.0119	17370	0.034
	Int	W24x68	W14x257	4234108.8	0.00298	12659	809470	0.0119	19899	0.034

3.2.5 Dynamic Properties of LA 9-Story

The dynamic properties of the LA 9-story structure modeled for the study were calculated in a modal analysis by *Perform.* Table 3.5 provides the period, T_i, and the mode shape, ϕ_i, for the first five modes of vibration.

Table 3.5: Periods and Mode Shapes for First Five Modes of Vibration

	T_1 (sec)	T_2 (sec)	T_3 (sec)	T_4 (sec)	T_5 (sec)
Period	2.31	0.86	0.49	0.32	0.22
	ϕ_1	ϕ_2	ϕ_3	ϕ_4	ϕ_5
Roof	1.000	1.000	0.968	-0.817	-0.523
9th	0.922	0.524	-0.151	0.837	1.000
8th	0.821	0.232	-0.933	1.000	0.108
7th	0.718	0.000	-0.989	-0.110	-0.990
6th	0.616	-0.404	-0.465	-0.975	-0.257
5th	0.507	-0.637	0.248	-0.867	0.833
4th	0.394	-0.739	0.804	0.029	0.632
3rd	0.282	-0.592	1.000	0.819	-0.352
2nd	0.171	-0.391	0.780	0.907	-0.836
1st	0.000	0.000	0.000	0.000	0.000

3.2.6 Dampers

The dampers that were used in the model are Maxwell dampers. This type of damper consists of a dashpot in series with a spring as illustrated in Figure 2.3. Analysis requires a damping coefficient, C_0, and a spring stiffness, k. The spring was given a large value of k so that the deformation in the device is limited to the damping component. The following section explains how to determine the force-velocity relationship, and the damping coefficient were determined.

3.2.6.1 Force-Velocity Relationship

An important purpose of this study is to determine if a system with nonlinear dampers is more suitable when subjected to certain types of ground motions. The dampers in the study were modeled using the following generalized form:

$$P(t) = C_0 \left| \frac{du}{dt} \right|^{\alpha} \operatorname{sgn}\left[\frac{du}{dt} \right] \qquad 3.8$$

where α is a real positive exponent that ranges from 0.1 to 2, and sgn is a signum function. When α is equal to unity the damper is linear. The computer program *Perform* requires the force-velocity relationship of the nonlinear damper element to be defined by six linear segments. When entered into *Perform,* the force-velocity relationship look similar to that illustrated in Figure 3.14.

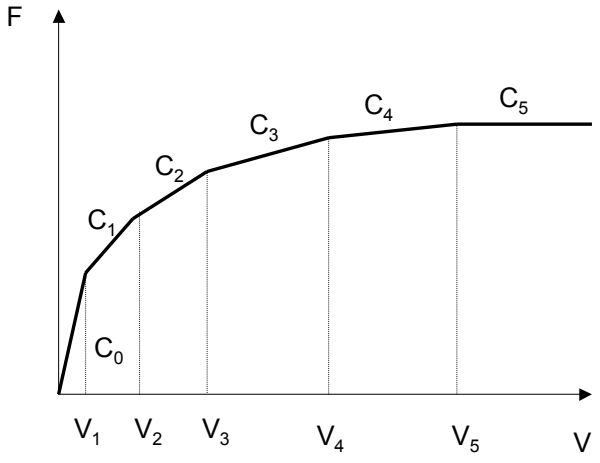

Figure 3.14: Force-Velocity Relationship for Nonlinear Damper in *Perform*

The force-velocity relationship for the damper illustrated in Figure 3.14 is the same when the damper is in compression or tension. It is also important to note that the damper force unloads along the same curve by which it is loaded.

3.2.6.2 Nonlinear Damping Coefficient

An objective of this study was to compare linear dampers with nonlinear dampers in their ability to improve the response of structures when subjected to different types of earthquakes. In order to make accurate conclusions, the dampers must be equivalent in some respect. In this study, an equal energy concept was implemented to make the linear and nonlinear dampers equivalent.

The force-displacement relationship for a linear and nonlinear viscous fluid damper is illustrated in Figure 3.15. Note that the plot of the relationship has different shapes for the different values of α. At the frequency of loading used to create the loops the enclosed areas for the various dampers are all equal, but the value of the damping coefficients are all different.

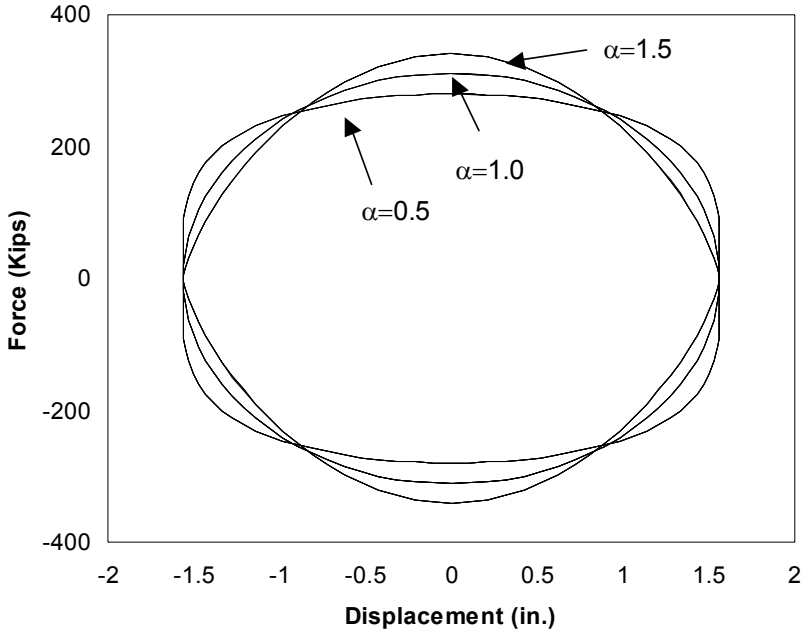

Figure 3.15: Force-Displacement Relationship for Linear and Nonlinear Viscous Fluid Dampers

From the force-displacement relationship, the work done per cycle can be determined at a given amplitude and frequency. According to Hanson and Soong (2001), the work done per cycle by a linear damper is given by

$$W_D = \pi\omega C_L u_{\max} = \pi F_D u_{\max} \tag{3.9}$$

where F_D is the axial force in the damper when u_{max} is the maximum displacement in the damper, ω is the frequency of the harmonic loading, and C_L is the damping coefficient. The work done per cycle by a nonlinear damper is given by

$$W_D = \lambda C_{NL} u_{\max}^{1+\alpha} \omega^{\alpha} = \lambda F_D u_{\max} \tag{3.10}$$

where

$$\lambda = 4 \times 2^{\alpha} \frac{\Gamma^2\left(1+\frac{\alpha}{2}\right)}{\Gamma(2+\alpha)} \tag{3.11}$$

where α is the damping exponent in Equation 3.8 and Γ is the gamma function. The gamma function is defined as

$$\Gamma(x) = \int_0^{\infty} u^{x-1} e^{-u} du \tag{3.12}$$

and can be simplified to

$$\Gamma(x) = (x-1)! \tag{3.13}$$

if x is an integer.

The first step in selecting the appropriate damping coefficients for the nonlinear dampers is to determine the damping coefficients for the linear dampers. The damping coefficients for the linear dampers are selected by satisfying the following equation:

$$\xi_i = \frac{\phi_i^T C \phi}{2\omega_i \phi_i^T M \phi} \tag{3.14}$$

where ξ_i is the ratio of critical damping for the i^{th} mode, ϕ_i is the mode shape, ω_i is the frequency, M is the mass matrix for the structure, and C is the damping matrix. Using trial and error, the coefficients for the damper at each floor of the structure are determined in order to produce a desired level of critical damping. These coefficients are

determined only using the 1st mode of vibration because it is assumed that the damping in the higher modes will be large and therefore the effects of the higher modes will be insignificant.

Once the coefficients for the linear dampers are found, the following equation is used to determine the nonlinear damper coefficients:

$$C_{NL} = C_L \frac{\pi}{\lambda} (u_{\max} \omega)^{1-\alpha} \qquad 3.15$$

Hanson and Soong (2001) derived Equation 3.15 by setting the work done for each type of damper equal to each other. It is important to note that this equation is a function of maximum displacement and frequency of vibration. In this study, the maximum displacement was varied to produce 1% and 5% story drift, while the frequency was set as the first modal frequency of the structure. It should also be noted that Equation 3.15 is only valid under steady state harmonic response.

Figure 3.16 displays the force-velocity relationship for linear and nonlinear dampers which when placed in the LA 9-story model produced a 10% critical damping ratio. The plot shows the difference in the relationship when the nonlinear dampers are calibrated for 1% and for 5% drift.

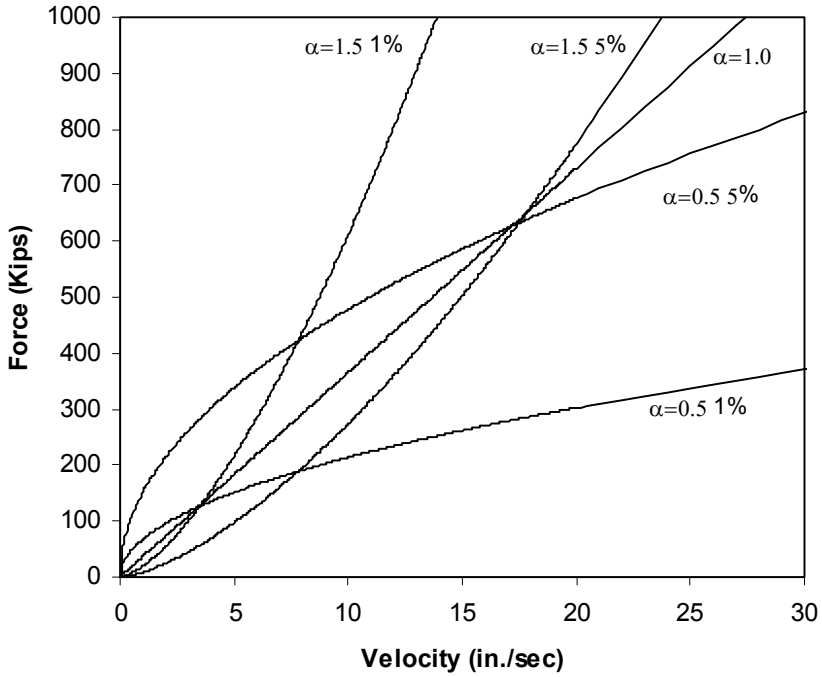

Figure 3.16: Force-Velocity Relationship for Dampers with Different Calibration Constants

Once the damper element was modeled, it needed to be incorporated into the model of the structure. The model in this study is a moment-resisting frame and, in actual structures, the dampers are normally placed in the gravity frame using a chevron bracing system. Therefore, the dampers were added to the moment-resisting frame by creating a separate outrigger frame with chevron braces and dampers. The lateral degrees of freedom of the outrigger frame were slaved to the lateral degrees of freedom of the moment-resisting frame at the respective floors. Slaving two different degrees of freedom to each other causes them to both displace equal amounts. In the absence of dampers, no stiffness is added to the structure by the outrigger frame. It has been assumed for the initial portion of the study that the chevron braces used in the damper frame were not allowed to yield.

One final point to note about the damping of the structure is that there was no inherent damping added to the structure. Inherent damping is the structural material's natural ability to dissipate energy when loaded with repeated cycles. There are many questions

as to the correct method for modeling inherent damping; these questions would add other parameters to the study. Therefore, in this study, it is assumed that any inherent damping that actually exists was included in the added damping.

3.2.7 P-Delta Effects

When structures are loaded laterally in combination with gravity forces, a second order effect, known as the p-delta effect, is present. This effect can significantly influence the response of the structure and must be considered in the model. Most analysis programs, including *Perform,* allow the modeler to choose whether or not to consider p-delta. The easiest way to do this, which was done in this study, is to add a p-delta column to the model. This column consists of a rigid bar for every story. The lateral degree of freedom of each end of the rigid bar is slaved to the respective floors. The gravity load for half of the building at each floor is then applied to the respective rigid bar. P-delta effects will then be turned off for every element in the structure except for the p-delta columns.

The reason for this approach is that the p-delta effect is a function of the axial load at a story. When applying the gravity loads to the moment frame, the loads are only for a tributary area equal to half a bay width if the moment frame is the exterior frame. However, the p-delta loads cause secondary moments and thus are only resisted by the moment frame. If there are only two moment frames in each direction, then the tributary area will be half the area of each floor. Therefore, the moment frame will be loaded with gravity loads and the p-delta column will be loaded with the p-delta loads.

It is important to note that when calculating base shear for the structure, the shear in the p-delta column at the base is included. The base shear for the p-delta column can be found using the following equation:

$$V_{p-d} = \frac{P}{h}\delta \qquad 3.16$$

where P is the axial force in the column if tension is considered positive, h is the story height, and δ is the first story displacement.

3.3 Procedure

3.3.1 IDA Procedure

Incremental Dynamic Analysis (IDA) was used in this study to investigate structural behavior when different types of dampers are placed in the structure and are subjected to different types of earthquake forces. In this study, the IDA procedure involved using nonlinear dynamic analysis to subject the LA model with a certain type of damper to 12 different earthquakes. Six of these earthquakes were classified as near-field earthquakes. Each earthquake was scaled to 20 different levels of intensity, which is measured by the design level spectral acceleration at the first fundamental period of the structure for 10% critical damping. The intensities ranged from 0.1g-2.0g and varied by increments of 0.1g. It is important to note that a value of $S_a(T_1,10\%)$ is unrealistically high, but was considered in this study so that a full range of structural behavior could be investigated.

As a result, 240 nonlinear time history analyses were performed on each building with a different damper variation. For each of these analyses, four different response measures were recorded; they are the Park and Ang damage index, peak interstory drift ratio, peak base shear, and residual displacement. Each of the response measures was then plotted versus earthquake intensity for all of the ground motions. These plots are called IDA curves.

The IDA curves are used to examine the following:

- System behavior changes as earthquake intensity increases
- System behavior changes when subjected to different earthquakes, including near-field and non near-field earthquakes,

- Behavior changes when the damping system changes
- Differences between the different response measures

3.3.2 Response Measures

The response measures used in the study were the Park and Ang damage index, peak interstory drift ratio, peak base shear, and residual deformation. The Park and Ang damage index and peak interstory drift were selected because they are both relatively easy to use and both provide reasonable characterization of damage. Peak base shear was selected because while increased damping can decrease deformation response, which may decrease damage, it can increase base shear at the same time. If the base shear is increased excessively, the increased damping becomes ineffective. Therefore, it is important to measure the base shear.

3.3.2.1 Park and Ang Damage Index

The Park and Ang index is presented in the following form:

$$DI_{PA} = \frac{u_{\max}}{u_{mon}} + \frac{\beta E_H}{F_y u_{mon}} \tag{3.17}$$

where u_{mon} is the maximum deformation capacity of the system under a monotonically increasing lateral deformation, $u_{\max}$ is the maximum deformation, E_H is the irrecoverable hysteretic energy, F_y is the yield strength of the system, and β is a calibration constant.

This damage index is a local index and the following weighted average of the local indices was used to find the DI for each story

$$DI_{story} = \frac{\sum_i DI_i E_i}{\sum_i E_i} \tag{3.18}$$

where DI_{story} is the story damage index, DI_i is the Park and Ang damage index for each member, and E_i is the amount of energy dissipated by member *i*. Once the DI is found for each story, the total DI for the structure can be determine using the following:

$$DI_{structure} = \frac{\sum_i DI_i^{story} E_i^{story}}{\sum_i E_i^{story}} \qquad 3.19$$

where $DI_{structure}$ is the story damage index, DI_i^{story} is the Park and Ang damage index for each story, and E_i^{story} is the amount of energy dissipated by story *i*.

3.3.2.2 Peak Interstory Drift Ratio and Peak Base Shear

Interstory drift ratio (IDR) and base shear are relatively simple to calculate. IDR can be described as the difference between the displacements of floors in a story normalized by the story height. For this study, *Perform* output the IDR for each story and for the total building.

Base shear is the sum of the lateral forces found in a structure's first-story members. In this study the dampers were included in the frame with chevron braces and it was important to include the lateral forces found in the damper braces. Figure 3.17 is an example of a building with a damper frame illustrating the lateral forces in the first story members. The calculation of base shear also includes the contribution made by the p-delta forces by using Equation 3.16.

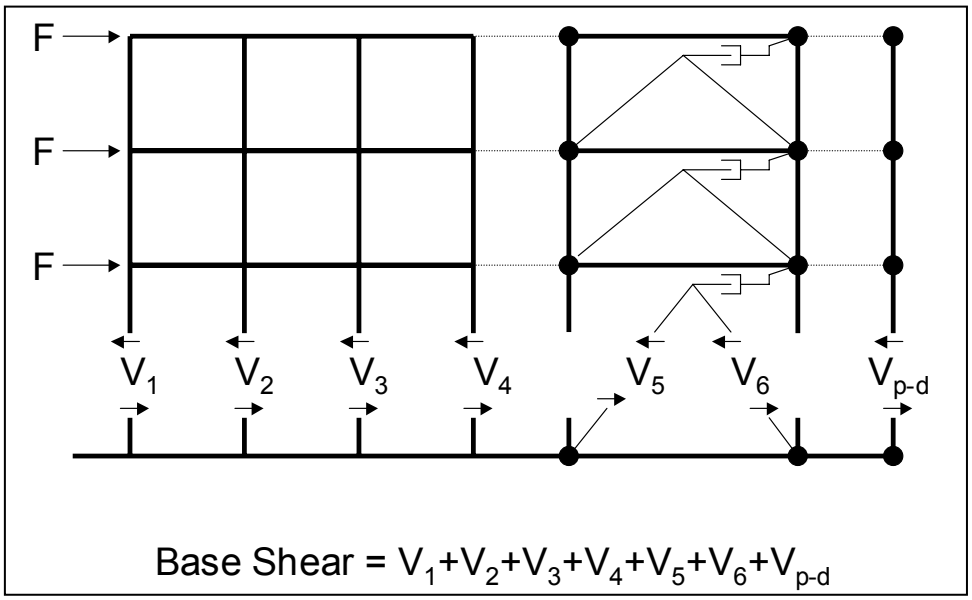

Figure 3.17: Example of Base Shear in a Structure

3.3.3 Residual Displacements

When plotting the results of the IDA procedure for several ground motions, it can be observed that every ground motion gives similar results up to a certain point, which will be referred to as the yield point. After the yield point there is a vast amount of variation between the curves. Ideally, if the equal displacement theorem holds true, all of the results should fall close together along a line extended from the linear portion of the curves. The equal displacement theorem suggests that the peak inelastic displacement will approximately equal the elastic peak response for any given intensity. This does not happen in the IDA curves, most likely due to residual displacements. Therefore, this study investigated the relationship between dispersion and residual displacements.

Residual displacements occur when a building is subjected to earthquake forces and is shifted in one direction and the building vibrates without returning to its original coordinates. Figure 3.18 is an example of a time history of the first-story drift of a building that experienced residual displacements when subjected the NF11 ground motion.

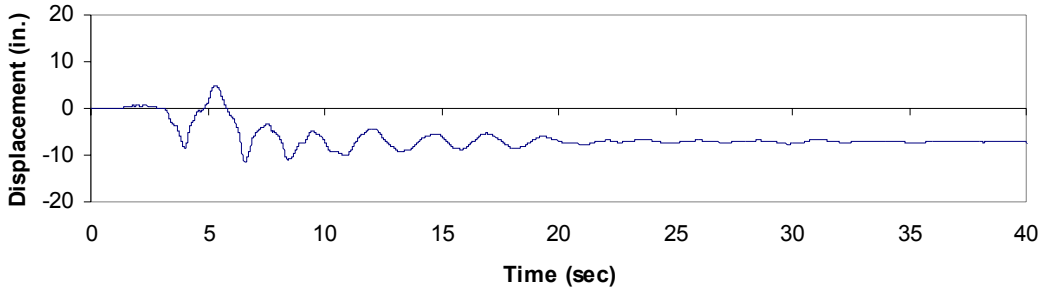

Figure 3.18: Time History Plot with Residual Displacement

In this study residual displacements were quantified for the first story of the building model by calculating a running average of the displacement. The increment of time over which the running average was calculated is equal to the first mode fundamental period of the building.

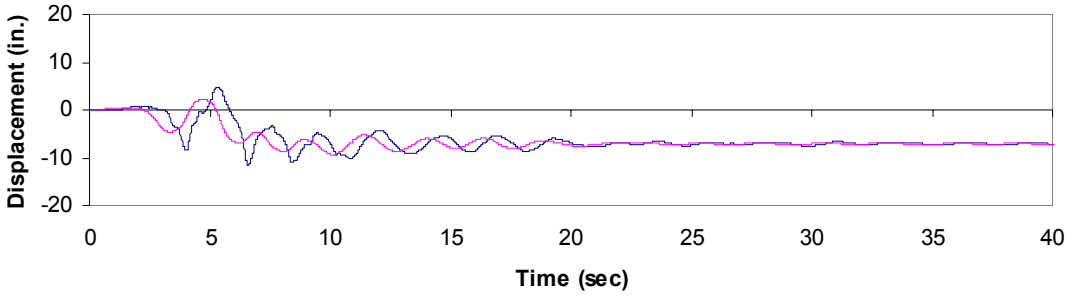

Figure 3.19: Time History Plot with Residual Displacement Measure

Figure 3.19 illustrates the running average superimposed on the same time history plot shown in Figure 3.18. The running average was used to determine if a certain damper type can limit residual displacements and to confirm that residual displacements are the cause of the dispersion in the IDA curves.

3.3.4 Ground Motions

Twelve ground motions were selected for the study. Six of the records used were defined as near-field earthquakes, which means that they are more impulse like motions than the other records. The following two sections discuss the ground motions selected for the study and how these motions were scaled for use in the IDA procedure.

3.3.4.1 Scaled Ground Motions Records

Table 3.6 lists the ground motions used in this study. Figure 3.20-Figure 3.31 display plots of each earthquake's acceleration versus time. These ground motions were selected from a larger group developed by Woodward-Clyde Federal Services of Pasadena, California as part of the System Performance Team for use in the SAC Joint Venture Steel Project Phase 2. The suites of ground motions developed by this group were to be used in the analysis of model steel buildings located in Los Angeles, Boston, and Seattle. Woodward-Clyde compiled both historic records and artificially generated time histories based on models of rupture mechanisms and wave propagation through the earth[2]. For this study, only the historic records of ground motions were used. The earthquakes labeled LA in Table 3.6 were selected from a set of ground motions for Los Angeles with a probability of exceedence of 10% in 50 years. The near-field ground motions labeled NF in Table 3.6 were selected from a set of earthquakes that are representative of those found at a near fault site.

[2] http://nisee.berkeley.edu/data/strong_motion/sacsteel/ground_motions.html

Table 3.6: Ground Motions Used in Study

Title	Earthquake	Date	Location	PGA at Design $S_a(T_1,10\%)$	Scale Factor
LA01	Imperial Valley	5/19/40	El Centro Valley Irr Dist	0.346 g	0.752
LA07	Landers	6/28/92	Barstow-Vineyard & H	0.519 g	1.233
LA10	Landers	6/28/92	Yermo Fire Station	0.545 g	1.515
LA11	Loma Prieta	10/17/89	Gilroy Ary 3,Gilroy Sewage Plant	0.416 g	0.626
LA13	Northridge	1/17/94	Newhall, LA County Fire Station	0.739 g	1.091
LA17	Northridge	1/17/94	Sylmar, Olive View FF	0.315 g	0.553
NF01	Tabas	9/16/1978	Tabas Station	0.491 g	0.546
NF07	C. Mendocino	4/25/1992	Petrolia	0.220 g	0.458
NF09	Erizinican	3/19/1992	Erzinican Meteorological Station	0.218 g	0.505
NF11	Landers	6/28/1992	Lucerne	0.550 g	0.772
NF13	Northridge	1/17/1994	Rinaldi	0.506 g	0.569
NF19	Kobe	1/17/1996	Takatori	0.204 g	0.259

Included in Table 3.6 is the scale factor used to give each ground motion the design spectral acceleration at the first fundamental period of the structure for 10% critical damping, $S_a(T_1,10\%)=0.217g$. Also included is the peak ground acceleration (PGA) at $S_a(T_1,10\%)=0.217g$. This is the PGA of the ground motion once it has been scaled to the design spectral acceleration at the first fundamental period of the structure for 10% critical damping. The scaling procedure that was used in this study is further explained in Section 3.3.4.2.

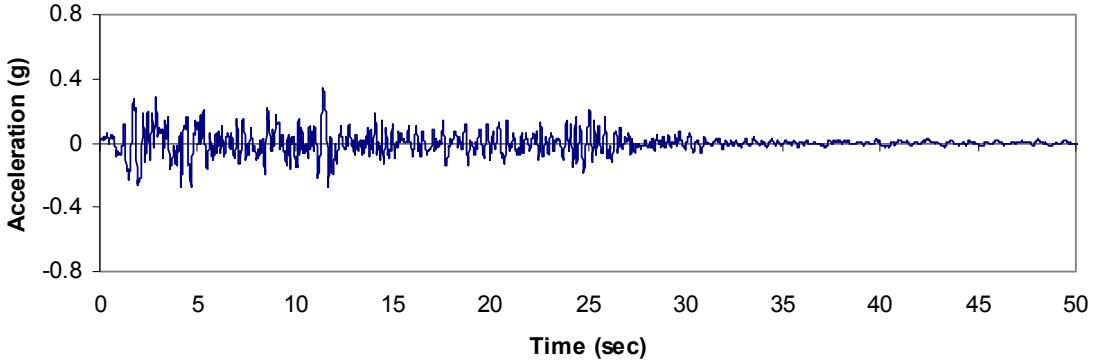

Figure 3.20: LA01-Imperial Valley

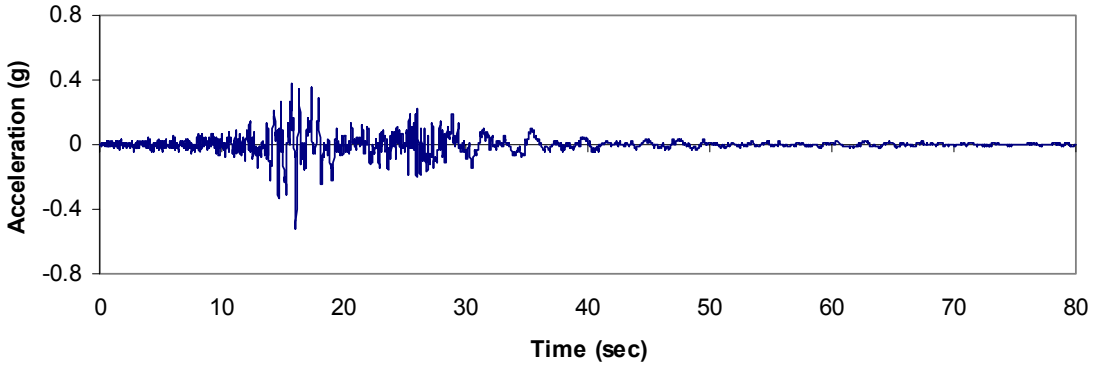

Figure 3.21: LA07-Landers

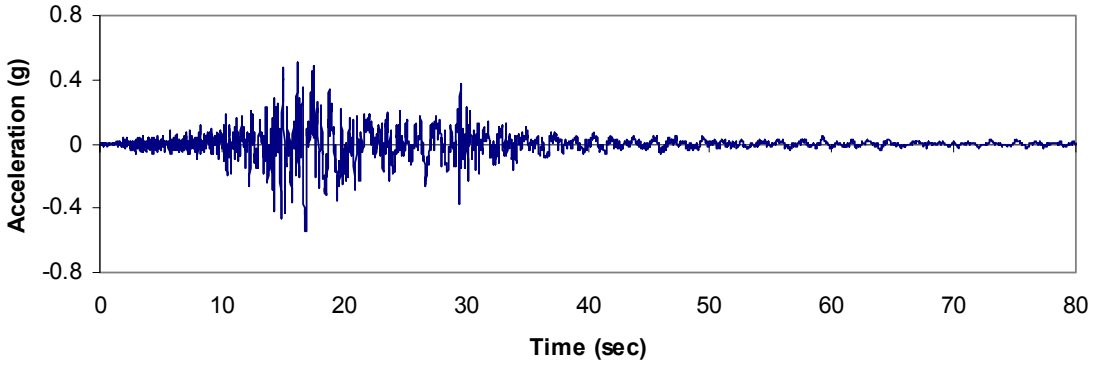

Figure 3.22: LA10-Landers

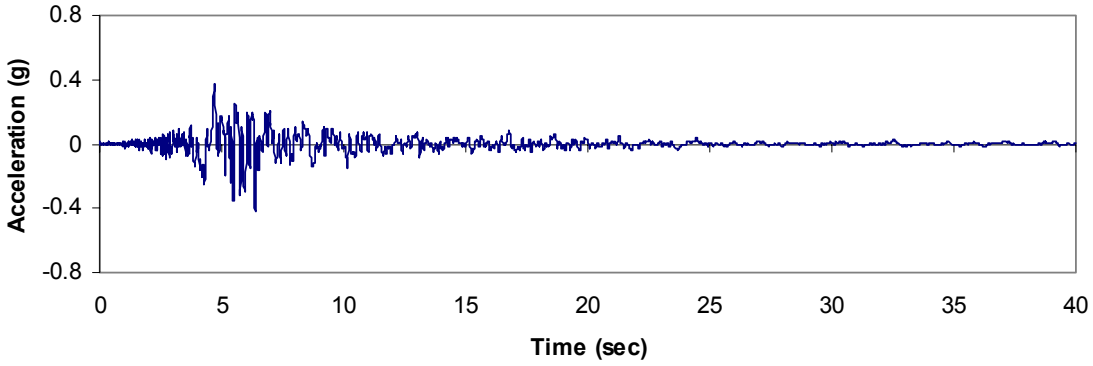

Figure 3.23: LA11-Loma Prieta

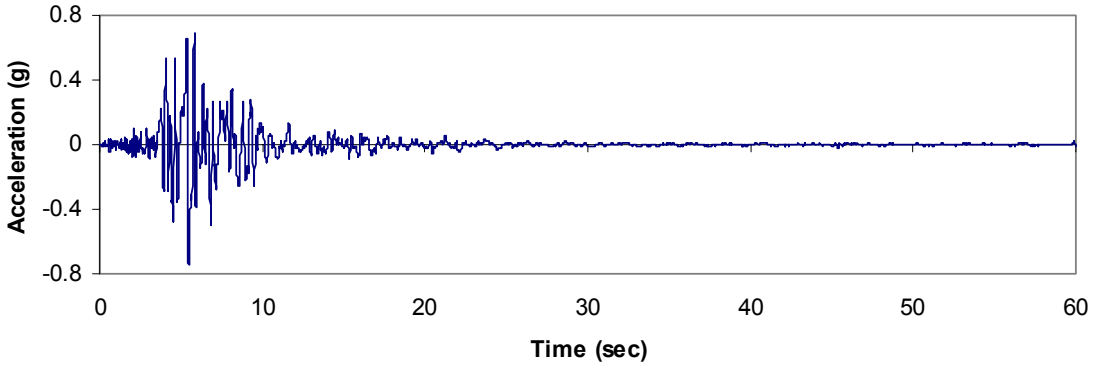

Figure 3.24: LA13-Northridge

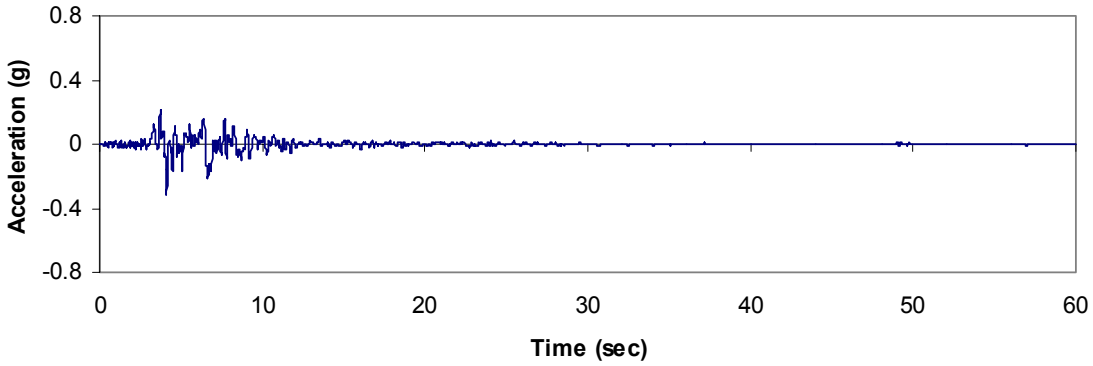

Figure 3.25: LA17-Northridge

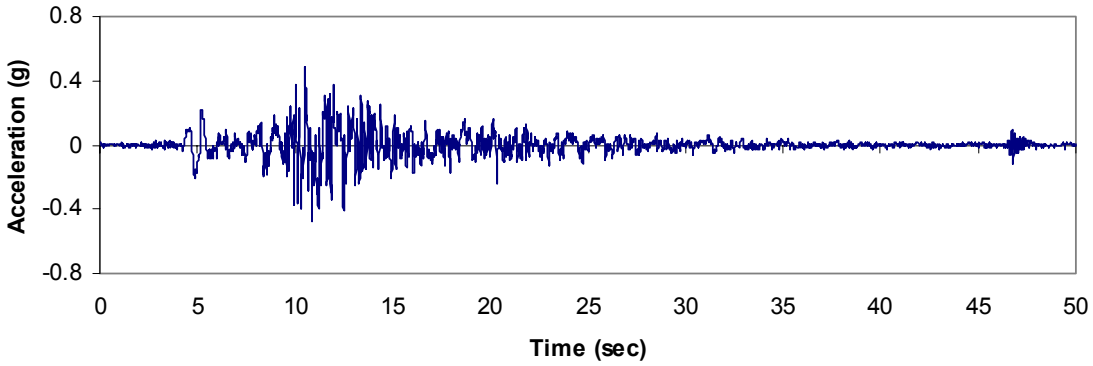

Figure 3.26: NF01-Tabas

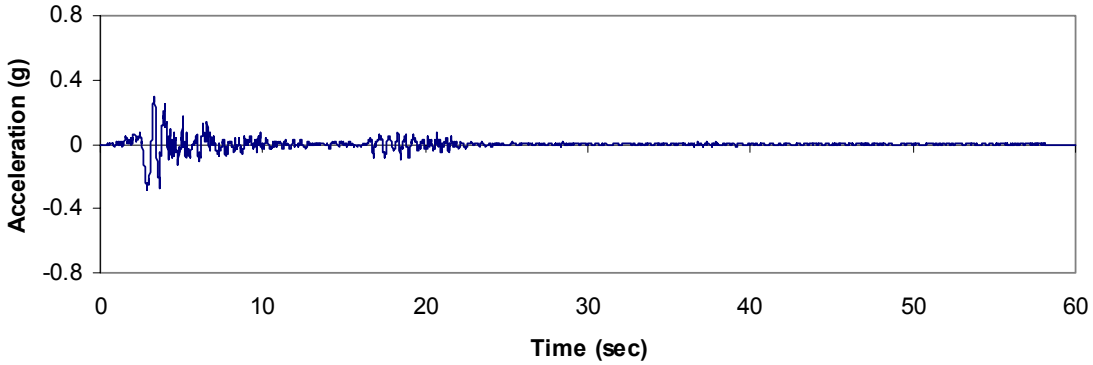

Figure 3.27: NF07-C. Mendocino

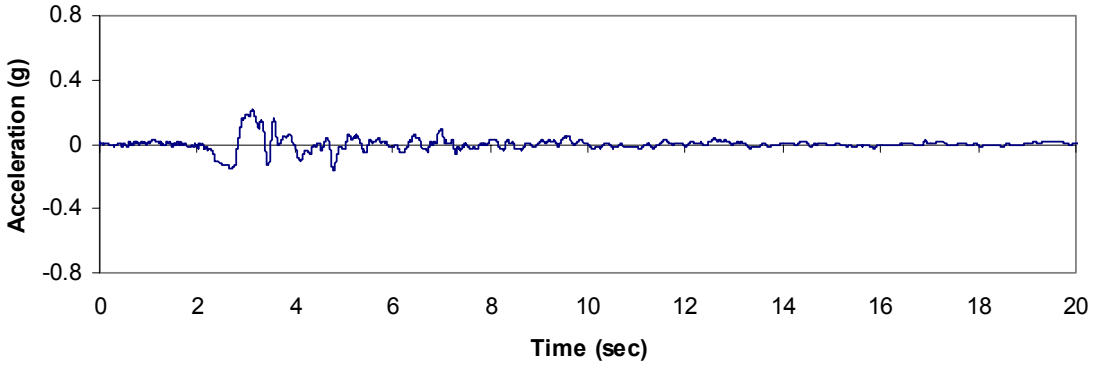

Figure 3.28: NF09-Erizinican

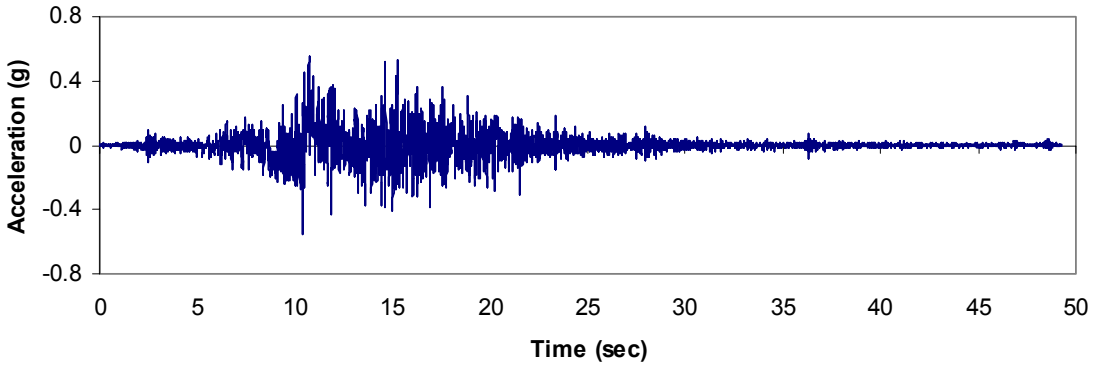

Figure 3.29: NF11-Landers

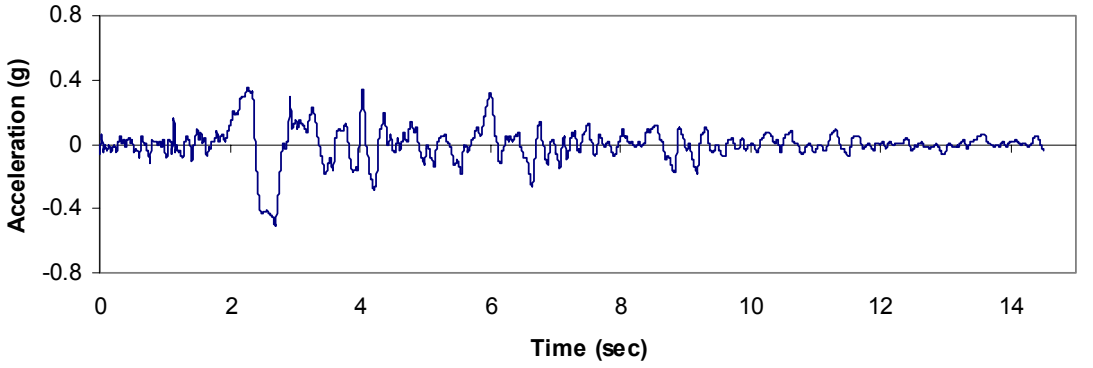

Figure 3.30: NF13-Northridge

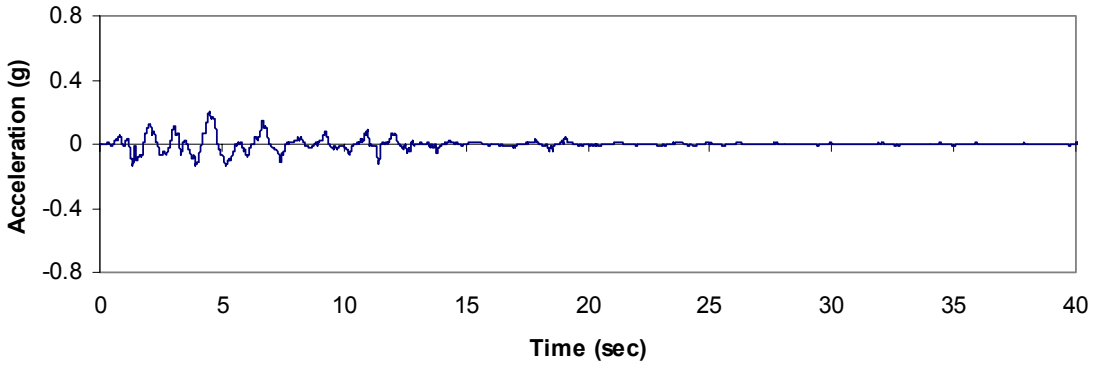

Figure 3.31: NF19-Kobe

3.3.4.2 Scaling the Ground Motions

The IDA procedure used in this study requires the ground motion records to be scaled. A major concern in scaling is assuring that the records are scaled in such a way that the response measures are valid. Vamvatsikos and Cornell (2002) suggest that for a moderate period steel frame with a response measure of interstory drift and a group of ground motions that range in magnitude from moderate to large, the best intensity measure is the first-mode spectral acceleration, $S_a(T_1)$. The value of $S_a(T_1)$ is that it is considered a good measure of the strength of the first-mode frequency, and the response of steel structures is dominated by the first mode. Another possible response measure that could be considered is peak ground acceleration (PGA); however, PGA is not a good measure of the strength of the first mode. More importantly, PGA cannot be correlated to spectral acceleration because as the ground motion intensity changes, the ratio of PGA to $S_a(T_1)$ also changes. Therefore, the ground motion records used in this study were scaled using the first-mode spectral acceleration for 10% of critical damping.

A program called *NONLIN* (Charney, 1997) was used to find the first-mode spectral acceleration for each of these records. *NONLIN* performed a response spectrum analysis for each record at 10% of critical damping. After an analysis was completed, an *Excel* output file is written that contains the period versus the spectral displacement. The spectral acceleration was then found using the following equation:

$$S_a = \omega^2 D \tag{3.20}$$

where $\omega = (2\pi/T)$, T is the period, and D is the displacement. Figure 3.32 (a) is a plot of the spectral accelerations versus period for the LA ground motions, while (b) does the same for the near-field ground motions.

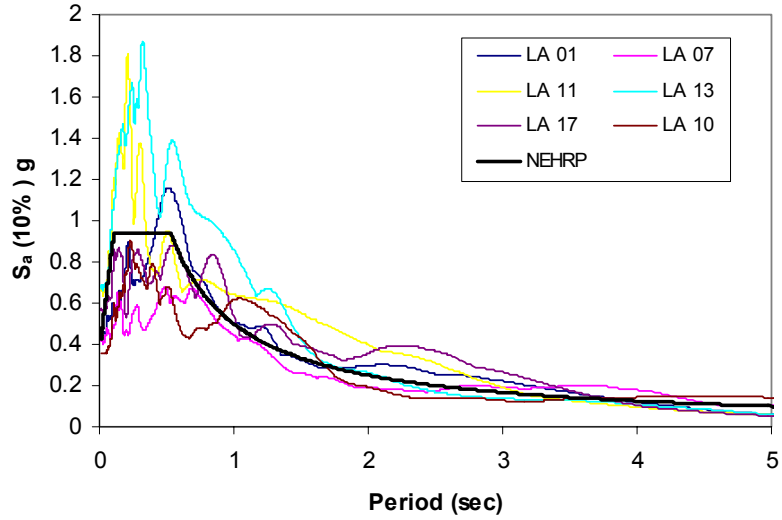

(a)

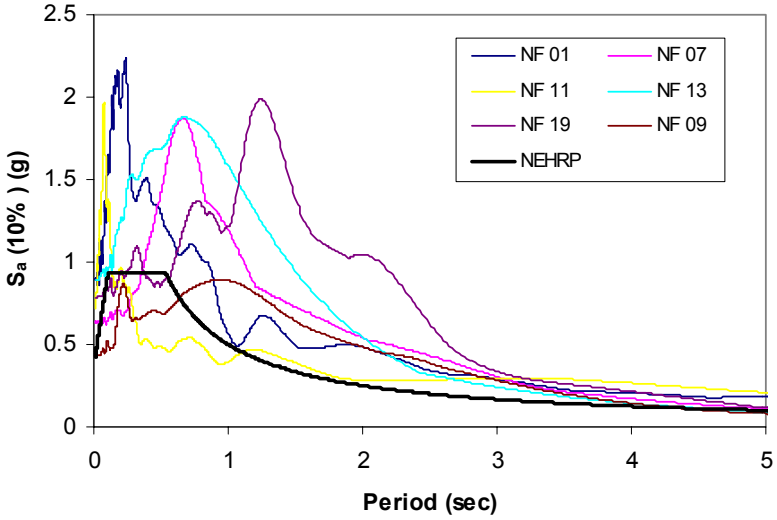

(b)

Figure 3.32 (a-b): Unscaled Response Spectrum for LA and NF Ground Motions

Included in Figure 3.32 is the design response spectrum defined by the *NEHRP Recommended Provisions for Seismic Regulation for New Buildings and Other Structures* (FEMA, 2000). It is important to note that the design response spectrum as defined in Chapter 4 of the *NEHRP* provisions is for 5% of critical damping. To modify this for

10% critical damping, the spectrum was divided by the damping coefficient, B_D=1.2, found in Table 13.3.3.1 of the Provisions. This design spectrum was used to obtain the base first-mode spectral acceleration by which all of the records were scaled, up or down, to different intensities. The first period of the building in this study is 2.30 seconds. For this period the design value of $S_a(T_1,10\%)$ is 0.217g and each of the records used was scaled so that all have this value at T_1. This is illustrated for the LA and NF ground motions in Figure 3.33 (a-b).

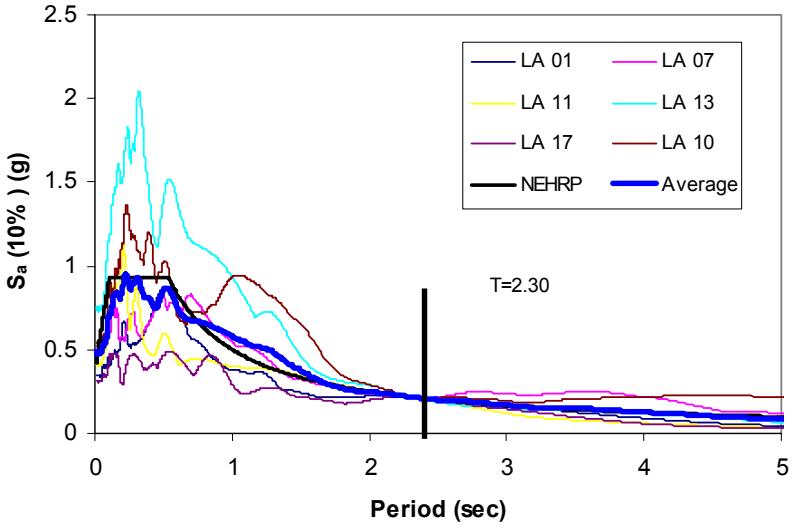

(a)

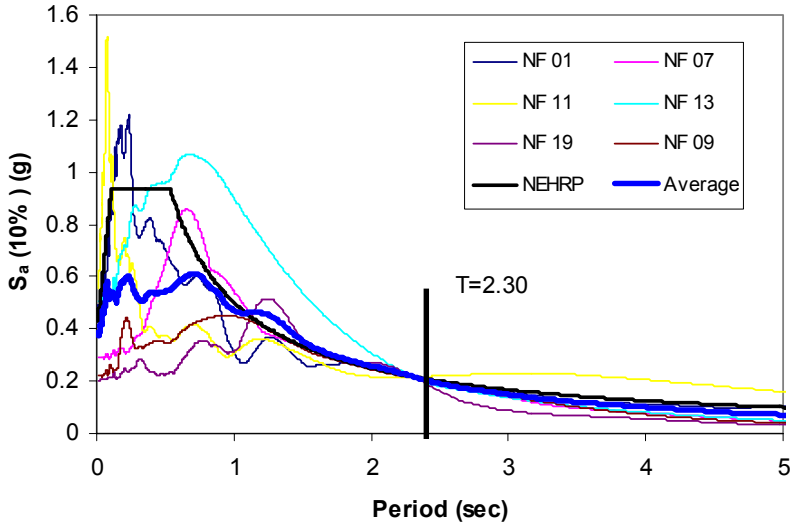

(b)

Figure 3.33 (a-b): Scaled Response Spectrum for LA and NF Ground Motions

Once the scaled ground motions were found, *Perform* has the ability to further scale them so that the intensity can be varied from 0.1g-2.0g by 0.1g increments.